Combined Winds and Turbulence Prediction System for Automated Air-Traffic Management Applications

Jung-Hoon Kim[1], William N. Chan[2], Banavar Sridhar[2], and Robert D. Sharman[3]

NASA Ames Research Center/Oak Ridge Associated Universities (ORAU), Moffett Field, California[1]

NASA Ames Research Center, Moffett Field, California[2]

National Center for Atmosphere Research (NCAR), Boulder, Colorado, USA[3]

Journal of Applied Meteorology and Climatology

Submitted 21 August 2014

Revised 19 December 2014

Accepted 29 January 2015

**Corresponding Author*: Dr. Jung-Hoon Kim, NASA Postdoctoral Program Fellow, Aviation Systems Division, NASA Ames Research Center, Mail code: 210-10, Moffett Field, CA, 94035-1000, United States.

Phone: +1-650-604-0293, Fax: +1-650-604-2316

E-mail: jung-hoon.kim@nasa.gov; jhkim99@me.com

Abstract

A time-lagged ensemble of Energy Dissipation Rate (EDR)-scale turbulence metrics is evaluated against in situ EDR observations from commercial aircraft over the contiguous United States and applied to Air-Traffic Management (ATM) route planning. This method uses the Graphic Turbulence Guidance forecast methodology with three modifications. First, it uses a convection-permitting scale (Δx = 3 km) Weather and Research Forecast (WRF) model to capture cloud-resolving scale weather phenomena. Second, turbulence metrics are computed for multiple WRF forecasts that are combined at the same forecast valid time, resulting in a time-lagged ensemble of multiple turbulence metrics. Third, probabilistic turbulence forecasts are provided based on the ensemble results, which are applied to the ATM route planning. Results show that the WRF forecasts match well with observed weather patterns and the overall performance skill of the ensemble turbulence forecast compared with the observed data is superior to any single turbulence metric. An example Wind-Optimal Route (WOR) is computed using areas experiencing ≥ 10% probability of encountering severe-or-greater turbulence. Using these turbulence data, lateral turbulence avoidance routes starting from three different waypoints along the WOR from Los Angeles international airport to John F. Kennedy international airport are calculated. The examples illustrate the tradeoff between flight time/fuel used and turbulence avoidance maneuvers.

1. Introduction

Previous studies of Wind-Optimal Routes (WORs) and turbulence impacts to the National Airspace System (NAS) have been conducted separately. This work aims to develop turbulence forecasts that can be used to evaluate how turbulence information affects WORs. Previous work has not explicitly accounted for turbulence when developing those routes though researchers have separately examined how pilots avoid areas of turbulence.

Several researchers have developed strategies for using WORs for Air-Traffic Management (ATM). Ng et al. (2012) developed optimal flight trajectories that minimized flight time and fuel burn by computing minimum-time routes in winds on multiple flight levels. Palopo et al. (2010) conducted a simulation of WORs and the impact on sector loading, conflicts, and airport arrival rates using a method developed by Jardin and Bryson (2001). Jardin and Bryson (2012) continued their research in this area by computing minimum-time flight trajectories using analytical neighboring WOR in the presence of a strong jet stream with winds of up to 80 m s^{-1}.

Prior research shows pilots seek to avoid areas of turbulence, and the impact of those maneuvers to ATM has been documented. Krozel et al. (2011) studied the maneuvers pilots made when they encountered Clear-Air Turbulence (CAT). They showed the pilot's response to CAT depended on factors such as aircraft type and company policies. In that study, they looked at turbulence maneuvers for the next 50 miles of flight and found that descending to a smooth flight level to be the usual tactical solution. Ignoring CAT near a jet stream of strong winds to achieve minimum-time routes may result in flight and fuel savings that cannot be fully realized due to a pilot's unwillingness to traverse turbulent areas to reach the maximum tail winds. Research shows two-thirds of all severe CAT occurs near the jet stream (Lester 1994). Turbulence information can also aid in the development of routes around convective systems. Ng et al. (2009) calculated convective weather avoidance routes considering the probability of pilot deviation using a model based on radar data. The model used by them and others to predict pilot behavior around convective systems, the Convective Weather Avoidance Model (CWAM), uses ground-based radar information to determine areas of convection where pilots will likely avoid (Delaura and Evans 2006). CWAM is currently used by NASA's Dynamic Weather Routing tool to create in-flight routing around convective weather and has been evaluated in field studies in collaboration with American Airlines (McNally et al. 2012). However, such a model can miss regions of Convectively Induced Turbulence (CIT) outside the convective clouds.

To address the lack of turbulence information in WOR applications, a predictive model of aviation-scale turbulence, such as the Graphical Turbulence Guidance (GTG) product (Sharman et al. 2006; Kim et al. 2011) in which an ensemble of turbulence diagnostics are computed can be used to modify the WOR solution. The turbulence diagnostics in turn are based on forecasts from a numerical weather prediction (NWP) model or ensemble of NWP models. Steiner et al. (2013) reviewed ensemble-based forecasting techniques and state that ensemble forecasting can be applied to turbulence. They also point out that probabilistic forecasts are appropriate for ATM strategic planning as they may provide guidance about the uncertainty associated with weather-related phenomena. Here, time-lagged ensemble NWP forecasts are used to drive ensembles of turbulence diagnostics to provide probabilistic information about turbulence likelihood. And in order to better predict the effects of convection as well as provide better representation of mountain wave and clear-air turbulence sources, a high-resolution (3 km horizontal grid spacing) NWP model is implemented. Further, each computed turbulence diagnostic is scaled to energy dissipation rate (EDR = $\varepsilon^{1/3}$ $m^{2/3}$ s^{-1}) as an aircraft-independent atmospheric turbulence metric. EDR is defined as the rate of the turbulent kinetic energy (TKE) transfer from large-scale to small-scale eddies. The large-scale eddies in atmosphere are inherently unstable. These large eddies break up and cascade down to smaller-scale eddies until the viscous dissipation becomes dominant and the TKE is converted to heat. The model-derived EDR metric is consistent with in situ EDR estimates currently available from several fleets of commercial airliners including B767s, B757s and B737s (Cornman et al. 1995; Sharman et al. 2014), which is convenient for forecast verification. The in situ EDR metric can be related to traditional turbulence intensity based on pilot-reported categories of “light (LGT)”, “moderate (MOD)”, and “severe (SEV)” by appropriate considerations of aircraft type and flight conditions (Sharman et al. 2014). For reasons discussed in Sharman et al. (2014), EDR is the preferred atmospheric turbulence unit for aviation-scale observations and forecasts.

The following sections describe the methodology and procedures for creating new turbulence forecasts. A comparison of these new forecasts with observed radar reflectivity and automated in situ EDR data is presented to assess the reliability and accuracy of the forecasts. Finally, as an example of turbulence application to ATM, WORs are computed from Los Angeles International Airport (LAX) to John F. Kennedy International Airport (JFK) with and without a turbulence forecast.

2. Methodology and procedures of the turbulence forecasts

From a meteorological perspective, small-scale turbulent eddies that directly affect commercial aircraft at cruising altitudes are generated by a number of possible sources. For example, strong vertical shears above and below a jet stream core, inertial instability due to anticyclonic shear and curvature flow, and the gravity wave emissions via geostrophic adjustment in the jet stream exit region are well-known turbulence generation mechanisms near an upper-level jet/frontal system (e.g., Lane et al. 2004; Kim and Chun 2010, 2011; Knox et al. 2008). Mountain wave breaking frequently causes aviation turbulence over complex topographic regions (e.g., Lane et al. 2009; Sharman et al. 2011, 2012). Flow deformation, gravity wave breaking, and thermal-shear instability near the various convective systems are also important sources for aviation turbulence (e.g., Lane et al. 2003; Lane and Sharman 2008, 2014; Kim and Chun 2012; Kim et al. 2014; Trier and Sharman 2009; Trier et al. 2010). To take into account these many turbulence generation mechanisms as well as uncertainties in the NWP model forecasts, a combination of several turbulence metrics due to different mechanisms and from different forecasts is essential, and is more reliable than using a single diagnostic or simple rule-of-thumb predictor (e.g., Sharman et al. 2006; Kim et al. 2011; Gill 2014; Gill and Stirling 2013). In addition, a convection-permitting high-resolution numerical weather prediction model is more useful to capture small-scale turbulent eddies induced by convective activity or other turbulence sources.

This new turbulence forecast method is a sequence of four different processes, which is summarized below.

1) A high-resolution NWP forecast model is used to produce 3D meteorological data such as u, v, and w wind components, potential temperature (θ), pressure (p), humidity, and cloud mixing ratios at a given valid time. Time-lagged ensembles are constructed from the forecast fields for different lead-times but valid at the same time.

2) Ten aviation turbulence metrics, each based on combinations of horizontal and/or vertical gradients of 3D meteorological variables from the NWP model, are calculated.

3) The ten metrics from the different time-lagged forecasts are mapped into a common atmospheric turbulence-scale (EDR-scale) based on the assumed log-normal (random) distributions.

4) All EDR-scale metrics are combined to produce both deterministic and probabilistic turbulence forecasts using different weights as a function of turbulence forecasting skill of each metric and is used to modify the WORs.

a. Weather model

In the first step, the WRF-ARW model version 3.5, is used as the weather forecast model in this study. This model uses a finite-difference method for non-hydrostatic and fully compressible prognostic equations on an Arakawa-C grid and terrain-following vertical sigma levels (Skamarock and Klemp 2007). The WRF-ARW model has been successfully applied to understand possible generation mechanisms of severe turbulence cases under different environmental weather conditions (e.g., Trier and Sharman 2009; Trier et al. 2010; Kim and Chun 2010; 2012; Kim et al. 2014). Design of the WRF-ARW model is the same as National Oceanic and Atmospheric Administration (NOAA) high-resolution rapid refresh HRRR (http://ruc.noaa.gov/hrrr/) operational system. The horizontal domain covers the entire CONUS (Figs. 1 and 2). The horizontal grid spacing is 3 km, and model top is at 20 hPa with 50 vertical layers, which leads to be about 500 m vertical grid spacing in the Upper-Troposphere and Lower-Stratosphere (UTLS). Rayleigh damping for the *w*-wind component is applied in a sponge layer of uppermost

5-km from the model top. Subgrid-scale microphysical processes are parameterized using the Thompson et al. (2004) scheme. Longwave and shortwave radiation parameterizations use the Rapid Radiative Transfer Model (RRTM; Mlawer et al. 1997). Land Surface Model (LSM) providing upward fluxes at surface for the Planetary Boundary Layer (PBL) scheme is parameterized by Rapid Update Cycle (RUC) LSM (Smirnova et al. 2000). Subgrid-scale vertical mixing is parameterized by the Mellor-Yamada-Janjić (MYJ) scheme (Janjić 2002) not only in the PBL but also in free atmosphere by solving the 1.5 order Turbulent Kinetic Energy (TKE) equation (Mellor and Yamada 1982).

The longest forecast time of each model run is six hours, and the frequency of model output is 15 minutes, which is also the same as the HRRR. Initial and boundary conditions use hourly reanalyses data over the CONUS from the 13-km Rapid Refresh (RAP) model domain. The spin-up time of the model is about 30 minutes, which is somewhat faster than other regional models, likely because the hydrometeors are already enhanced in the initial condition of the RAP 13-km domain by assimilating the ground-based radar observation (http://ruc.noaa.gov/hrrr/). The model was run using the Pleiades supercomputer at the NASA Ames Research Center (http://www.nas.nasa.gov/hecc/). The wall-clock run-time using 500 cores took an hour to complete one model run with 15-minute forecast outputs up to six hours. The run-time could be decreased by using more computer resources, but the one-hr run time should be adequate for most operational purposes.

The following are example comparisons of the WRF-ARW model forecasts against the observed meteorology for two selected cases. The first case is for the 36 hour period from 0600 UTC 7 to 1800 UTC 8 September 2012 when several turbulence encounters were observed near convective systems over the CONUS (Figs. 1a and b). At 1730 UTC 7 September, several convective clouds begin to develop along a surface cold front elongated from the Great Lakes to Kansas. Locally isolated convective clouds also developed ahead of the cold front along a squall line over Illinois and Indiana (Fig. 1a). Several turbulence events with EDRs ≥ 0.22 m$^{2/3}$ s^{-1} scattered in the Northeastern CONUS, reported by the in situ measurements from commercial aircraft, were probably due to the convection well to the west (Fig. 1). An EDR of 0.22 corresponds to moderate turbulence for large commercial aircraft by Sharman et al. (2014). Note this value is lower than the current ICAO standard value form "moderate" of 0.40 m$^{2/3}$ s^{-1}. Some of these EDR reports are located within convective cloud, while others are outside of visible deep convection as confirmed by the radar data in Figs. 1a and b. As the upper-level trough deepened, clusters of thunderstorms along the eastward-moving cold front shown in Fig. 1b swept out the entire eastern and southern CONUS regions on 7-8 September 2012.

These radar observations are reasonably well captured by the WRF-ARW model. In particular, forecasted echo tops along an elongated front from the Great Lakes to Kansas in Figs. 1c and d are qualitatively similar to the observed radar data in Figs. 1a and b. This gives confidence that the large-scale flow-generated convective clouds responsible for aircraft-scale turbulence are well reproduced by the ARW-WRF model in this study. Considering that the upper-level westerly jet stream is dominant during this period over the northeastern CONUS (see Figs. 8 and 9 later), turbulence scattered in this area during this period is likely to be generated by interactions between a deep convection-induced disturbance and jet stream-related instabilities.

The second example case is the 12 hours period (0600-1800 UTC) on 31 December

2011 when strong mountain wave activity is dominant due to the passage of a strong northwesterly jet stream over the Rocky mountain region. As shown in Fig. 2a, there are no well-developed convective systems over the CONUS, which is also reliably simulated by the ARW-WRF model (Fig. 2b). Some clouds with echo tops lower than 20,000 ft (hereafter FL200) appear over Nebraska, but those are far away from the observed turbulence encounters over the mountain regions in both Colorado and Utah (Fig. 2b). Strong northwesterly jet flow embbeded on a planetary short wave is passing over the complex mountain ranges of the western US (Fig. 2c). This in turn generates mountain waves that propagate vertically up to the tropopause, as evidenced by the complicated wave patterns of vertical velocity over the western mountains (Fig. 2d). During this period, turbulence encounters ≥ 0.22 $m^{2/3}$ s^{-1} observed by in situ EDR occur not near the convective system but over the Rocky mountain regions, which is mainly due to the interactions between the mountain waves and the background wind (Figs. 2c and d). Some of elevated in situ reports are far downstream of the mountains near the border between Colorado and Nebraska, which may be related to the downstream propagation of the lee wave and/or jet-stream related gravity waves that trigger instabilities.

Due to the multiple turbulence-causing mechanisms in these and other cases, combinations of turbulence metrics based on various turbulence generation mechanisms are essential to accurately forecast turbulence events. In all, a total of 270 turbulence encounters ≥ 0.22 $m^{2/3}$ s^{-1} EDR value were observed over the CONUS by the in situ EDR measurements during two selected periods, and these are available for verification of the turbulence forecasts.

b. Turbulence diagnostics

For the second step, ten different turbulence diagnostics are computed. Although the horizontal grid spacing of 3 km was used in the WRF-ARW model, the horizontal size of aircraft-scale turbulence (normally 10-1,000 m) is still much smaller (i.e., subgrid-scale). However, aircraft-scale turbulence can be diagnosed by assuming that small-scale turbulent eddies directly affecting commercial aircraft cascade down from large-scale (resolved scale) disturbances and are revealed as high values of the turbulence diagnostics (e.g., Sharman et al. 2006; Kim et al. 2011; Williams and Josh 2013). In this study, three different time-lagged ensemble members of weather forecasts (e.g., 1.5, 2.5, and 3.5-hr) were used to calculate the turbulence diagnostics for each valid time. The upper-level turbulence diagnostics selected have relatively high performance skill in previous and current operational upper-level GTG systems (e.g., Sharman et al. 2006). The ten turbulence metrics used are the WRF-produced subgrid-scale turbulent kinetic energy (*SGS TKE*), Frehlich and Sharman's (2004) EDR (*FS EDR*), square of total deformation (*DEFSQ*), absolute value of horizontal divergence (*ADIV*), square of vertical component of relative vorticity (*VORTSQ*), absolute value of vertical velocity (*ABW*), two-dimensional frontogenesis function on pressure coordinates (*F2D*), Brown turbulence index 1 (*Brown1*), nested grid model turbulence index (*NGM*), and the horizontal temperature gradient (*HTG*). These diagnostics were then divided by the gradient Richardson number (Ri_g) (Sharman 2013). Detailed formulations of the diagnostics are provided in Appendix A.

c. EDR mapping technique

This third step maps each turbulence diagnostic to a common atmospheric turbulence scale. The previously described turbulence diagnostics have different numerical formulations and units. However, a final turbulence forecast should be on a common scale such as the EDR. EDR is independent of aircraft type or size and mapping turbulence diagnostics into the EDR scale allows them to be compared with observed in situ EDR measurements. So, all of the turbulence diagnostics calculated were mapped to the EDR metric. In this study, we assumed that each model-derived turbulence diagnostic has a log-normal distribution that can be derived from the best fit function of the log-scale Probability Density Function (PDF) especially for larger values of turbulence diagnostics for longer period of time (Sharman et al. 2014).

Figures 3 and 4 show an example of nine EDR-scale metrics from a 2.5-hr forecast product averaged over three different flight levels of FL300, FL350, and FL400 valid at 1730 UTC 7 September 2012 and at 1830 UTC December 2011, respectively. In general, most of the EDR-scale metrics for relatively larger values (orange shading; EDR ≥ 0.22 m$^{2/3}$ s^{-1}) are consistent with the turbulence encounters ≥ 0.22 m$^{2/3}$ s^{-1} values in the observed in situ EDR measurements in commercial flights both near the convective system for the first case (Fig. 3) and over the Rocky mountain regions for the second case (Fig. 4). And, relatively lower values of EDR-scale metrics also capture well the smooth areas of the in-flight bumpiness ≤ 0.01 m$^{2/3}$ s^{-1} values depicted as gray-dotted lines over the CONUS. But, there are some places where some EDR-scale metrics over estimate some smooth regions of in situ EDR reports of bumpy areas, which increases the false alarm ratio (FAR), and therefore should be considered as a score function in the ensemble of metrics.

d. Ensemble of EDR-scale turbulence metrics

The final step combines all EDR-scale metrics into deterministic and probabilistic turbulence forecasts. At a given forecast time, we used a total 30 of EDR-scale metrics [i.e., ten different turbulence metrics from three different NWP forecasts (e.g., 1.5, 2.5, and 3.5 hr forecast data)] for the ensemble EDR forecasts. For the deterministic ensemble EDR, 30 EDR-scale metrics are combined into a weighted ensemble mean (e.g., Figs. 5a and c) using different weighting functions of each metric (W_i), as follows.

$$Ensemble\ EDR(x,y,z) = \sum_{i=1}^{N} W_i EDR_i(x,y,z)\,, \quad i = 1,2,3,\ldots,N = 30. \qquad (1)$$

$$W_i = \frac{(AUC_i/RMSE_i)^2}{\sum_{i=1}^{N}(AUC_i/RMSE_i)^2}\,, \quad i = 1,2,3,\ldots,N = 30. \qquad (2)$$

Here, the weighting function in Eq. (2) is as a combination of the Root Mean Square Error (RMSE) and Area Under Curve (AUC) of the Probability Of Detection "yes" for the EDR value ≥ 0.22 $m^{2/3}\ s^{-1}$ and "no" for the EDR value smaller than 0.01 $m^{2/3}\ s^{-1}$ (PODY and PODN) statistics for each EDR-scale turbulence metric. Details of the AUC metric will be presented in the next section.

An attribute of a probabilistic forecast product is that it takes into account the uncertainties in the underlying NWP forecast model. In this study, at the given valid time a 3D probabilistic ensemble for Severe-Or-Greater (SOG)-level turbulence areas are calculated by counting how many EDR-scale individual turbulence metrics out of the total 30 metrics have EDR values ≥ 0.47 $m^{2/3}\ s^{-1}$ at each grid point in the model, which is depicted in Figs. 5b and d. Here, the threshold is adapted from the median value of in situ EDR-severe PIREP pairs for longer period over the CONUS (Sharman et al. 2014).

Figure 5 shows a snapshot of (a and c) a deterministic ensemble EDR using Eq. (1) and (b and d) a probabilistic forecast for SOG-level turbulence for the two cases. These are averaged over flight levels FL300, FL350, and FL400 using three time-lagged ensemble members of forecast data (1.5-3.5 hr) valid on 1730 UTC September 2012 (upper) and on 1830 UTC December 2011 (lower). The results show the deterministic ensemble EDR for larger values (orange shading; EDR $\geq$ 0.22 $m^{2/3}$ s^{-1}) mostly agrees well with the observed in situ EDR measurements $\geq$ 0.22 $m^{2/3}$ s^{-1} (blue asterisks) in Fig. 5 (left). For the probabilistic forecast (Fig. 5 right), the 10% SOG-level turbulence probability is also well correlated with the observations (blue asterisks) especially over western Michigan and northern Ohio on 7 September 2012 (Fig. 5b) and over the western mountains in Utah and Colorado on 31 December 2011 (Fig. 5d). Considering that the background (natural) probability for SOG-level turbulence encounters in UTLS is less than 0.1% (Sharman et al. 2006; 2014), the forecasted 10% SOG-level turbulence probability (orange color shading) in Fig. 5 (right) is regarded as significantly higher than the background SOG-level turbulence potential in UTLS. The choice of the 10% SOG probability threshold is arbitrary, but has similar features to the 50% MOG probability in this study. But, the reason we emphasize the 10% SOG turbulence probability in this figure is because in the aviation community avoiding SOG turbulence is regarded as a hard constraint that should be always avoided, while any MOG threshold is a soft constraint that aircraft may penetrate by employing the fasten seatbelt sign.

3. Evaluation of deterministic EDR metrics

In this section, the forecasted EDR-scaled turbulence diagnostics shown in Figs. 3 and 4 and the deterministic ensemble EDR shown in Fig. 5 (left) are compared with in situ EDR reports to objectively obtain their statistical skill. The forecasting performance skills are calculated using the probability-of-detection "yes" for the EDR ≥ 0.22 m$^{2/3}$ s^{-1} (PODY) versus "no" for the EDR ≤ 0.01 m$^{2/3}$ s^{-1} (PODN). This technique has been used for the verification of various turbulence forecasts (e.g., Sharman et al. 2006; Kim et al. 2011). If the forecasted value of each EDR-scaled turbulence metric at the nearest grid point to the observed MOG location around ±30 minutes (30 minute time window) of the valid time is higher (lower) than the in situ EDR, the $Y_{for}Y_{obs}$ ($N_{for}Y_{obs}$) was counted as shown in Table 1 and Eq. (3);

$$PODY = \frac{Y_{for}Y_{obs}}{Y_{for}Y_{obs} + N_{for}Y_{obs}}, and \ \ PODN = \frac{N_{for}N_{obs}}{Y_{for}N_{obs} + N_{for}N_{obs}}. \qquad (3)$$

and if the forecasted EDR value near the null observation is smaller (higher) than the observed in situ EDR, the $N_{for}N_{obs}$ ($Y_{for}N_{obs}$) was counted. These procedures were applied to a total of 270 turbulence events ≥ 0.22 m$^{2/3}$ s^{-1} EDR value [hereafter moderate-or-greater (MOG) EDR] and 55,150 smooth events with EDR ≤ 0.01 m$^{2/3}$ s^{-1} on both 7-8 September 2012 and 31 December 2011. This process was repeated through 20 different thresholds that ranged from EDR values of 0 to 1, resulting in 20 PODY and PODN statistics for both the ensemble EDR and EDR-scale turbulence metrics.

Figure 6 (left) shows example *PODY-PODN* plots constructed from these 20 threshold values for the DEFSQ /Ri diagnostic for (a) 7-8 September 2012, (b) 31 December 2011, and (c) both cases, for various forecast lead times (1.5-5.5 hr). Values of area under these curves (AUC) are a measure of the forecast performance skill (e.g., Sharman et al. 2006; Kim et al. 2011). An AUC = 1 is a perfect forecast [i.e., a turbulence metric can perfectly discriminate all MOG EDR and smooth events and/or a turbulence metric has a perfect forecast for MOG EDR without any false alarm ratios (1-PODN)]. Figure 6 (d)-(f) show PODY-PODN plots for five other turbulence metrics (SGS TKE/Ri, FS EDR/Ri, DEFSQ/Ri, ADIV/Ri, and VORTSQ/Ri) from 2.5-hr forecast data, for the two cases as in (a)-(c). Also shown in Fig. 6 are PODY-PODN curves for ensemble EDRs defined from eqn. (3) using three different forecast lead times (1; using 1.5-3.5 hrs data, 2; using 2.5-4.5 hrs data, and 3; using 3.5-5.5 hrs data).

In Fig. 6, the ensemble EDRs have generally higher forecasting performance skill than any of single EDR-scale turbulence metric. Especially for the first case on 7-8 September 2012 (Figs. 6a and b), the ensemble EDRs have AUC values around 0.83-0.84, which is superior to the AUC values of single EDR-scale metrics of between 0.69-0.81. This result is the same as in the second case on 31 December 2011 (Figs. 6c and d). This is consistent with the previous results of turbulence forecasts that the integrated turbulence metrics provide superior forecasting skill than any single turbulence metric at least in terms of the AUC performance metric (e.g., Sharman et al. 2006; Kim et al. 2011; Gill 2014; Gill and Stirling 2013). To assess the stability of these results we randomly picked half fractions of the 270 turbulence and 55,150 smooth events and re-evaluated them 100 times. The minimum and maximum AUC values of the final deterministic EDR forecast are 0.77 and 0.9, respectively, which is about a –9% to +6% difference around the obtained performance (0.85) in Fig. 6e and f. Although this does not imply that the performance would be better or not in other cases, the variability of the obtained skill is statistically stable at least in these cases, and this performance is consistent with the previous studies (e.g., Sharman et al. 2006, Kim et al. 2011).

Overall, the forecast skill for the second case is generally higher than those in the first case. This is somewhat expected since the nature of the turbulence events for the first case are associated with convective systems (Fig. 1) which are not as reliably forecasted as those in the second case near the mountain areas (Fig. 2). This implies that the fidelity of the cloud-resolving scale WRF model is higher in the case of mountain wave-induced turbulence than in the convectively driven turbulence case.

All of the AUC and RMSE values as well as an example of the weighting scores derived from the Eq. (2) for the ten turbulence metrics are shown in Table 2. In general, as we expected, the RMSE values increase in all EDR-scale metrics, as the forecast-lead time increases from 1.5-hr to 5.5-hr according to the decreasing fidelity of the weather forecast. The combination of the AUC and RMSE values according to the Eq. (1) gives the weighting scores such that the FS EDR/Ri metric has the largest contribution for the ensemble EDR with the highest AUC and lowest RMSE values, while the F2D/Ri metric is the smallest contribution. The SGS TKE metric also has a small contribution because it is from the Planetary Boundary Layer scheme in the WRF-ARW model, which cannot be expected to perform well in stably-stratified shear-flow turbulence characteristic of the UTLS.

4. Example of turbulence application to ATM

In this section, an example WOR based on lateral deviations only using turbulence information for ATM planning is described. With a correct choice of initial heading angle, the minimum-time path in the presence of wind (i.e., WOR) can be obtained by applying Pontryagin's Minimum Principle (Bryson and Ho 1975) to determine the analytic solution for the control parameter (here, the heading angle of cruising aircraft;

ψ) in the governing equations of the simplified horizontal aircraft motions over a spherical Earth, as follows.

$$\frac{d\phi(t)}{dt} = \frac{V_a\, cos\psi(t) + U(\phi,\theta,z)}{R\, cos\theta(t)}, \qquad (4)$$

$$\frac{d\theta(t)}{dt} = \frac{V_a sin\psi(t) + V(\phi,\theta,z)}{R}, \qquad (5)$$

Here, ϕ, θ, and ψ are longitude, latitude, and heading angle of the aircraft, and U and V are wind components, respectively. R is the Earth's radius that Earth is assumed to be a sphere and $R >> z$, and V_a is the airspeed of aircraft, assumed to be 250 m s^{-1}. The analytic solution for the control parameter (ψ) that minimizes the total travel time from the departure to arrival is

$$\frac{d\psi(t)}{dt} = -\frac{F_{wind}(t)}{R\, cos\theta(t)}. \qquad (6)$$

A full derivation of the analytic solution including $F_{wind}(t)$ in Eq. (6) is described in Appendix B.

A shooting method is used to find the initial heading angle. First, the great circle heading angle (ψ_{GC}) between the departure and arrival points is used as the first guess of the initial heading angle [$\psi(t_0)$]. And then, we solved the Eqs. (4), (5), and (6) using an explicit Euler forward integration scheme, $[\alpha(t+1) = \alpha(t) + \Delta t \frac{d\alpha(t)}{dt}, where\ \alpha = \phi, \theta, and\ \psi.]$, from LAX [$\phi(t_0)$, $\theta(t_0)$, $\psi(t_0)$] to JFK [$\phi(t_f)$, $\theta(t_f)$, $\psi(t_f)$] with Δt = 60 seconds (1 min). This process is iterated with different initial heading angles [$\psi(t_0)$] within two boundary values (ψ_{GC} – 22.5° and ψ_{GC} + 22.5°) until the distance between a waypoint of the WOR trajectory and JFK is minimized.

Figure 7 shows example WORs without consideration of turbulence effects from LAX to JFK along with plots for horizontal winds and probabilistic ensemble EDR for SOG at FL350 and their cross-sections valid at 1730 UTC 7 September 2012 and 1830 UTC 31 December 2011. In the first case (Fig. 7a), a flight cruising at FL350 along the WOR would take 238 minutes (3 hr 58 min), which is 2 minutes less than the elapsed time along the great circle route with wind (sky-blue line). In Fig. 7a, the WOR would experience a total of 52 minutes of areas ≥ 10% probability of encountering SOG-level turbulence over northern Indiana, Ohio, and western Pennsylvania. In the vertical cross-section along this WOR (Fig. 7c), the 10% SOG-level turbulence areas seem to block all possible flight levels from FL260 to FL450 over these regions. This indicates that Lateral Avoidance Turbulence Routes (LTARs) would be better suited to avoid turbulence than vertical changes of the flight level in this case.

In Fig. 7b, the second case shows the same situation as in Fig. 7a with the WOR, taking 238 minutes and experiencing 20 minutes in the SOG-level turbulence areas from LAX to JFK, which is 2 minutes less elapsed time than the great circle route with wind (sky-blue line). And, in Fig. 7d, the turbulence potential areas are vertical from FL230 to FL450 near southern Colorado, which again implies that the LTARs would be a better choice than vertical avoidance. Fortunately, in the second case (Fig. 7b), only a small lateral deviation from the WOR (blue line) can entirely avoid the turbulence region.

To demonstrate quantitatively the effects of turbulence avoidance on the WOR routes, we use a probabilistic ensemble EDR ≥ 10% probability of encountering SOG-level turbulence (i.e., LTAR). The SOG-level is selected because it is considered a hard constraint that pilots should avoid due to aviation safety concerns. And, a 10% probability is chosen because it correlates well with observed in situ EDR reports greater than 0.22 $m^{2/3}$ s^{-1} already shown in Figs. 5b and d.

The LTAR can be determined by following the same approach for the optimization of the WOR with a different minimization condition or cost function (J), as follows.

$$J = \int_{t_0}^{t_f} \{C_t + C_r\, r(\phi, \theta, z)\} dt. \qquad (7)$$

Here, C_t and C_r are the cost coefficients of travel time and penalty areas along the LTAR, respectively. In this study, $r(\phi, \theta, z) = 1$ when the probabilistic ensemble EDR for SOG-level ≥ 10%, and elsewhere $r(\phi, \theta, z) = 0$ (e.g., Ng et al. 2011; Sridhar et al. 2010).

$$\frac{d\psi(t)}{dt} = -\frac{\{F_{wind}(t) + F_{turb}(t)\}}{R\, cos\theta(t)\, \{C_t + C_r\, r(\phi, \theta, z)\}}. \qquad (8)$$

Equation (8) is the solution for the control parameter (ψ) that minimizes the cost function by Eq. (7) from departure to arrival. A full derivation of the analytic solution including $F_{turb}\,(t)$ is given in Appendix B. Solving Eqs. (4), (5), and (8) using the same shooting method used for the WOR described earlier, gives us the LTAR (red and green lines in Fig. 8) from LAX to JFK for the first case. This LTAR can be initiated at the departure time, however, it would be preferable to delay such a maneuver until closer to the forecasted turbulence constraint, because the maneuver decision needs to consider several factors like confidence of the weather forecast.

In Fig. 8 (upper), the LTAR trajectory for the 10% SOG-level turbulence potential using 3.5-5.5 hr forecasts initiated from the departure (LAX) is depicted as a red line. The LTAR (red line) takes a total of 254 minutes flying time and used 6.7% extra time to entirely avoid the forecasted 10% SOG-level turbulence areas. Two other alternative LTARs were initiated 1.5 hrs (middle) and 2.5 hrs (lower) after departing LAX along the WOR (blue lines) with more recently updated forecasts data. An aircraft that follows the LTAR 1.5 hrs after departing LAX (middle in Fig. 8) has a flying time of 244 minutes, which saves 10 minutes more than that if it were to follow the LTAR initiated from the LAX (red line in upper in Fig. 8). However, if an aircraft follows an LTAR 2.5 hrs after departing LAX, when it is closer to more recently forecasted turbulence regions (lower in Fig. 8), it takes a total of 256 minutes of flying time. This is 2 minutes longer than the LTAR initiated from the departure (red line in upper figure in Fig. 8). Therefore, in this case, the most efficient LTAR is the one that begins its lateral detour 1.5 hrs after the departure (middle figure in Fig. 8). This takes 244 minutes from LAX to JFK, avoiding entirely all areas of SOG probability > 10%. Note that the example of LTARs shown in Fig. 8 may not be the most efficient maneuver, because there are several other ways to avoid the potential constraints of turbulence, such as tactical change of flight altitude and route just ahead of turbulence areas.

5. Summary and conclusions

In this paper, the time-lagged ensembles of the EDR-scaled turbulence diagnostics computed from the high-resolution WRF-ARW model are used in automated ATM route planning and three example applications for re-routing around turbulence are given. The new turbulence forecasting techniques can create both deterministic and probabilistic turbulence information using a sequence of four procedures. These include high-resolution weather modeling using time-lagged ensembles, calculation of reliable turbulence diagnostics on these grids, mapping of these metrics to an EDR-scale, and combining the predictions into a turbulence product. In the two cases presented here, 10 turbulence diagnostics derived from three time-lagged ensemble members are used to provide a total of 30 different turbulence forecasts. This system uses the operational GTG methodology with three modifications, which include the use of (1) a finer horizontal grid, (2) a time-lagged ensemble forecast with an ensemble of various turbulence metrics, and (3) probabilistic for ATM as opposed to deterministic turbulence information. Using a convection-permitting scale weather model with time-lagged ensemble members would be beneficial for the improved turbulence forecasts related to smaller-scale sources like convective system and mountain waves. Providing probabilistic ensemble EDRs is useful for ATM route planning and decision making.

The developed turbulence forecast was created and evaluated both for 7-8 September 2012 when several convective clouds developed along a surface frontal system that swept across the mid and eastern CONUS and for 31 December 2011 when a strong northwesterly jet stream generated mountain waves and disturbances over the Rocky Mountain region. The deterministic version of the EDR-scale turbulence forecast was verified against observed in situ EDR-scale turbulence estimates from several commercial aircraft. The new method was observed to have a higher forecasting skill than other single EDR-scale turbulence metrics.

A simple WOR and three LTAR applications were developed to show the utility of this forecast product for route planning applications. The results shown in Figs. 7 and 8 are summarized in Table 3. Using the WOR with ignoring turbulence maneuvers, a minimum-time path experiences areas ≥ 10% probability of encountering SOG-level turbulence for 52 minutes. Since in both example cases considered, the potential turbulence areas along the WOR are vertically deep, laterally deviating around the turbulence areas seems the best option to avoid turbulence in this case. It is found that to laterally detour around these potential areas of the turbulence from the departure airport (LAX) an aircraft would incur 16 minutes (6.7%) more travel time to fly to its destination (JFK) [LTAR 1 in Table 3 and red line in Fig. 8 (upper)]. Delaying the horizontal maneuver would result in either a savings of 10 minutes if the maneuver were delayed 1.5 hrs after leaving LAX [LTAR 2 in Table 3 and green line in Fig. 8 (middle)] or an extra 2 minutes if the maneuver was delayed by 2.5 hrs until the aircraft would get close to the turbulence potential regions [LTAR 3 in Table 3 and green line in Fig. 8 (lower)]. 10 minutes time saving in LTAR2 can be very significant because this reduction roughly equals to about 160 km less distance of flying and about 760 kg of fuel savings, which is a benefit for commercial airline operations.

Future work will use different thresholds instead of the 10% SOG probability to explore the tradeoffs between time/fuel used and penetrating certain portions of the turbulence area. In addition, when the fuel consumption model will be included in the cost function of Eq. (10), the current 2-D lateral turbulence avoidance route (LTAR) will be extended to 3-D maneuvers that minimize the fuel consumption and potentials of turbulence encounters during the total flight time. The strategic avoidance methodology suggested for turbulence herein can be also applied to other types of weather constraints such as icing, volcano ash, wind gust, and potential of contrail formation. Reducing the run-time would make the new method useful for tactical decisions such as near-term routing around convective weather as well. This can be accomplished by using data from a nowcast version of the GTG or output from a faster-running numerical model.

Acknowledgments

This work was supported by an appointment to the NASA Postdoctoral Program at the Ames Research Center, administrated by the Oak Ridge Associated Universities (ORAU) through a contract with NASA. We specially thank Matthias Steiner at NCAR, Ng Hok Kwan, Todd Farley, and Dallas Denery at NASA Ames Research Center for their invaluable peer reviews. We also thank the editor (Todd D. Sikora) and three anonymous reviewers for their invaluable comments that help to improve the manuscript.

Appendix A

1) SGS TKE: Subgrid scale turbulent kinetic energy (SGS TKE) is a turbulence-related variable that is directly produced by the weather forecast model. In the WRF model used, the Mellor-Yamada-Janjić planetary boundary layer parameterization (Janjić 2002) predicts local vertical turbulent mixing not only in the PBL but also in the free atmosphere through the Mellor-Yamada level 2.5 turbulence closure model:

$$\frac{\partial q^2/2(x,y,z)}{\partial t} = -\overline{u'w}(x,y,z)\frac{\partial U(x,y,z)}{\partial z} - \overline{u'w}(x,y,z)\frac{\partial V(x,y,z)}{\partial z} + \beta g \overline{\theta'_v w}(x,y,z) + \frac{\partial}{\partial z}\left(0.2\ell q \frac{\partial q^2/2}{\partial z}\right) - \varepsilon. \qquad (A1)$$

where $q^2/2$, u', w, U, V, β, g, θ_v, l, and ε are the subgrid-scale TKE, u and w the subgrid wind components, U and V the grid-resolved wind components, β = 1/273, the gravity acceleration (9.8 m s^{-2}), virtual potential temperature, mixing length, and energy dissipation rate as a function of TKE and mixing length (l), respectively. Variables under the bar are subgrid-scale vertical momentum and heat fluxes that are parameterized in the ARW-WRF model.

2) FS EDR: The EDR ($\varepsilon^{1/3}$) at given grid point is estimated from second-order structure functions for the resolved scale U and V wind components along horizontal directions by assuming the sensitivity to the structure functions in different NWP models is negligible at small-scales (Frehlich and Sharman 2004):

$$\varepsilon^{\frac{2}{3}}(x,y,z) = \frac{< \{q(x,y,z) - q(x,y,z+s)\}^2 >}{C_q(s) D_{REF}(s)}. \qquad (A2)$$

where q is U and V wind components, and s, $C_q(s)$, and $D_{REF}(s)$ are separation distance, correction function that takes into account NWP model spatial filter, and the reference structure function given by Lindborg (1999). <> bracket is the ensemble mean.

3) DEFSQ: Square of total deformation (*DEF*) that is sum of shear deformation and stretching deformation (e.g., Bluestein 1992).

$$DEF(x,y,z) = \left[\left\{\frac{\partial V(x,y,z)}{\partial x} + \frac{\partial U(x,y,z)}{\partial y}\right\}^2 + \left\{\frac{\partial U(x,y,z)}{\partial x} - \frac{\partial V(x,y,z)}{\partial y}\right\}^2\right]^{\frac{1}{2}}. \quad (A3)$$

4) ADIV: Absolute value of horizontal divergence (*DIV*).

$$DIV(x,y,z) = \frac{\partial U(x,y,z)}{\partial x} + \frac{\partial V(x,y,z)}{\partial y}. \qquad (A4)$$

5) VORTSQ: Square of vertical component of relative vorticity (*VORT*).

$$VORT(x,y,z) = \frac{\partial V(x,y,z)}{\partial x} - \frac{\partial U(x,y,z)}{\partial y}. \qquad (A5)$$

6) ABW: Absolute value of vertical velocity.

$$ABW(x,y,z) = |w(x,y,z)|. \qquad (A6)$$

7) F2D: Full 3-dimensional frontogenesis function simplified to two dimensions (F2D) in pressure coordinates using the thermal-wind relation (Bluestein 1992).

$$F2D(x,y,z) = \{\nabla_p \theta(x,y,z)\}^{-1}\left[-\left\{\frac{\partial\theta(x,y,z)}{\partial x}\right\}^2\left\{\frac{\partial U(x,y,z)}{\partial x}\right\}\right.$$

$$-\left\{\frac{\partial\theta(x,y,z)}{\partial y}\right\}\left\{\frac{\partial\theta(x,y,z)}{\partial x}\right\}\left\{\frac{\partial V(x,y,z)}{\partial x}\right\}$$

$$-\left\{\frac{\partial\theta(x,y,z)}{\partial x}\right\}\left\{\frac{\partial\theta(x,y,z)}{\partial y}\right\}\left\{\frac{\partial U(x,y,z)}{\partial y}\right\}$$

$$\left.-\left\{\frac{\partial\theta(x,y,z)}{\partial y}\right\}^2\left\{\frac{\partial V(x,y,z)}{\partial y}\right\}\right]. \qquad (A7)$$

Here, θ is potential temperature (K).

8) Brown1: Brown's index by Brown (1973) is a simplification of the original Richardson number tendency equation by Roach (1970) using the thermal wind relation and assuming the wind is approximately in gradient wind balance.

$$Brown1(x,y,z) = [0.3\{VORT(x,y,z) + f(x,y)\}^2 + DEF(x,y,z)^2]^{\frac{1}{2}}. \qquad (A8)$$

9) NGM1: Multiplication of horizontal wind speed and total deformation, similar to Ellrod's index (Reap 1996).

$$NGM1(x,y,z) = \{U(x,y,z)^2 + V(x,y,z)^2\}^{1/2} \times DEF(x,y,z). \qquad (A9)$$

10) HTG: Horizontal temperature gradient (*HTG*) provides inferences of the deformation and vertical wind shear via the thermal-wind relation (e.g., Buldovskii et al. 1976).

$$HTG(x,y,z) = \left[\left\{\frac{\partial T(x,y,z)}{\partial x}\right\}^2 + \left\{\frac{\partial T(x,y,z)}{\partial y}\right\}^2\right]^{\frac{1}{2}}. \qquad (A10)$$

Here, T is temperature (°C).

Appendix B

Pontryagin's Minimum Principle (Bryson and Ho 1975) is applied to the governing Eqs. (4) and (5) of the aircraft motion to determine the control parameter (heading angle of aircraft) that minimizes the cost function defined by Eq. (7) from the departure to arrival along the trajectory. The necessary condition for the control parameter and the optimal trajectory is that there exist continuously differentiable Lagrange multipliers (λ_Φ, λ_θ). Using these the Hamiltonian is then,

$$H = C_t + C_r\, r(x,y,z) + \left(\frac{\partial\lambda}{\partial\phi}\right)\left\{\frac{V_a\, cos\psi(t) + U(\phi,\theta,z)}{R\, cos\theta(t)}\right\}$$

$$+ \left(\frac{\partial\lambda}{\partial\theta}\right)\left\{\frac{V_a\, sin\psi + V(\phi,\theta,z)}{R}\right\}. (B1)$$

Therefore, the Euler-Lagrange equations are, as follows.

$$-\frac{d}{dt}\left(\frac{\partial\lambda}{\partial\phi}\right) = \frac{\partial H}{\partial\phi}$$

$$= \frac{\partial}{\partial\phi}\{C_r\, r(\phi,\theta,z)\} + \frac{1}{R\, cos\theta(t)}\left(\frac{\partial\lambda}{\partial\phi}\right)\left\{\frac{\partial}{\partial\phi}U(\phi,\theta,z)\right\}$$

$$+ \frac{1}{R}\left(\frac{\partial\lambda}{\partial\theta}\right)\left\{\frac{\partial}{\partial\phi}V(\phi,\theta,z)\right\}. \quad (B2)$$

$$-\frac{d}{dt}\left(\frac{\partial\lambda}{\partial\theta}\right) = \frac{\partial H}{\partial\theta}$$

$$= \frac{\partial}{\partial\theta}\{C_r\, r(\phi,\theta,z)\} + \frac{1}{R\, cos\theta(t)}\left(\frac{\partial\lambda}{\partial\phi}\right)\left\{\frac{\partial}{\partial\theta}U(\phi,\theta,z)\right\}$$

$$+ \left(\frac{\partial\lambda}{\partial\phi}\right)\frac{tan\theta(t)\,\{V_a\, cos\psi(t) + U(\phi,\theta,z)\}}{R\, cos\theta(t)}$$

$$+ \frac{1}{R}\left(\frac{\partial\lambda}{\partial\theta}\right)\left\{\frac{\partial}{\partial\theta}V(\phi,\theta,z)\right\}. \ (B3)$$

Under the condition that there is extremum for $t_0 \le t \le t_f$, the optimal heading angle should satisfy,

$$\frac{\partial H}{\partial \psi} = 0 \ \rightarrow tan\psi = \frac{\lambda_\theta \ cos\theta}{\lambda_\phi}. \qquad (B4)$$

The necessary condition for optimality is $H(t_f) = 0$, so the Lagrange multipliers are obtained when the Hamiltonian = 0, as follows.

$$\frac{\partial \lambda}{\partial \phi} = \frac{-\{C_t + C_r \ r(\phi,\theta,z)\} \ R \ cos\psi(t) \ cos\theta(t)}{V_a + U(\phi,\theta,z) \ cos\psi(t) + V(\phi,\theta,z) \ sin\psi(t)}. \qquad (B5)$$

$$\frac{\partial \lambda}{\partial \theta} = \frac{-\{C_t + C_r \ r(\phi,\theta,z)\} \ R \ sin\psi(t)}{V_a + U(\phi,\theta,z) \ cos\psi(t) + V(\phi,\theta,z) \ sin\psi(t)}. \qquad (B6)$$

Differentiate in right and left hand sides of Eq. (B4) with respect to time, and Eqs. (B2), (B3), (B5), and (B6) are substituted,

$$\frac{d\psi(t)}{dt} = -\frac{\{F_{wind}(t) + F_{turb}(t)\}}{R \ cos\theta(t) \ \{C_t + C_r \ r(\phi,\theta,z)\}}. \qquad (B7)$$

$$F_{wind}(t) = -sin\psi(t)cos\psi(t)\frac{\partial U(\phi,\theta,z)}{\partial \phi} + cos^2\psi(t)sin\theta(t)U(\phi,\theta,z)$$

$$+ cos^2\psi(t)cos\theta(t)\frac{\partial U(\phi,\theta,z)}{\partial \theta} - \frac{\partial V(\phi,\theta,z)}{\partial \phi}$$

$$+ sin\psi(t)cos\psi(t)sin\theta(t)V(\phi,\theta,z)$$

$$+ cos\psi(t)sin\psi(t)cos\theta(t)\frac{\partial V(\phi,\theta,z)}{\partial \theta} + V_a \ cos\psi(t)sin\theta(t)$$

$$+ cos^2\psi(t)\frac{\partial V(\phi,\theta,z)}{\partial \phi}. \qquad (B8)$$

$$
\begin{aligned}
F_{turb}(t) = &-sin\psi(t)cos\psi(t)sin\theta(t)V(\phi,\theta,z)C_r r(\phi,\theta,z) \\
&+ cos\theta(t)cos\psi(t)sin\psi(t)\frac{\partial V(\phi,\theta,z)}{\partial\theta}C_r r(\phi,\theta,z) \\
&- cos\theta(t)cos\psi(t)sin\psi(t)V(\phi,\theta,z)C_r\frac{\partial r(\phi,\theta,z)}{\partial\theta} \\
&+ V_a cos\psi(t)sin\theta(t)C_r r(\phi,\theta,z) + V_a sin\psi(t)C_r\frac{\partial r(\phi,\theta,z)}{\partial\phi} \\
&- \frac{\partial V(\phi,\theta,z)}{\partial\phi}C_r r(\phi,\theta,z) + V(\phi,\theta,z)C_r\frac{\partial r(\phi,\theta,z)}{\partial\phi} \\
&- sin\psi(t)cos\psi(t)\frac{\partial U(\phi,\theta,z)}{\partial\phi}C_r r(\phi,\theta,z) \\
&+ sin\psi(t)cos\psi(t)U(\phi,\theta,z)C_r\frac{\partial r(\phi,\theta,z)}{\partial\phi} \\
&+ cos^2\psi(t)sin\theta(t)U(\phi,\theta,z)C_r r(\phi,\theta,z) \\
&+ cos^2\psi(t)cos\theta(t)\frac{\partial U(\phi,\theta,z)}{\partial\theta}C_r r(\phi,\theta,z) \\
&- V_a cos\theta(t)cos\psi(t)C_r\frac{\partial r(\phi,\theta,z)}{\partial\theta} \\
&- cos\theta(t)cos^2\psi(t)U(\phi,\theta,z)C_r\frac{\partial r(\phi,\theta,z)}{\partial\theta} \\
&+ cos^2\psi(t)\frac{\partial V(\phi,\theta,z)}{\partial\phi}C_r r(\phi,\theta,z) \\
&- cos^2\psi(t)V(\phi,\theta,z)C_r\frac{\partial r(\phi,\theta,z)}{\partial\phi}.
\end{aligned}
$$

For the WOR that doesn't take into account the turbulence information, C_t = 1 and C_r = 0, which changes Eq. (B7) to Eq. (6). On the other hand, for the WOR with turbulence information (i.e., LTAR), C_t = 1, and C_r = 1 when the probabilistic ensemble

EDR forecast at given grid point for SOG-level turbulence ≥ 10%, while $C_r = 0$ when the turbulence potential is less than 10%.

References

Bluestein, H. B., 1992: *Principles of Kinematics and Dynamics.* Vol. I. *Synoptic–Dynamic Meteorology in Midlatitudes*. Oxford University Press, 431 pp.

Brown, R., 1973: New indices to locate clear-air turbulence. *Meteor. Mag.*, **102**, 347–360.

Bryson, A. E., and Ho, Y. C., 1975: *Applied Optimal Control*, Taylor and Fancis, Levittown, PA, 481 pp.

Buldovskii, G. S., Bortnikov, S. A., and Rubinshtejn, M. V., 1976: Forecasting zones of intense turbulence in the upper troposphere, *Meteor. Gidrol.*, **2**, 9–18.

Cornman, L. B., Morse, C. S., and Cunning, G., 1995: Real-Time Estimation of Atmospheric Turbulence Severity from In-Situ Aircraft Measurements, *J. Aircraft*, **32(1)**, 171-177.

DeLaura, R., and Evans, J., 2006: An Exploratory Study of Modeling En Route Pilot Convective Storm Flight Deviation Behavior. Preprints, *12th Conference on Aviation, Range, and Aerospace Meteorology*, Atlanta, GA, Amer. Meteor. Soc.

Frehlich, R., and Sharman, R. D., 2004: Estimates of turbulence from numerical weather prediction model output with applications to turbulence diagnosis and data assimilation. *Mon. Wea. Rev.*, **132(10)**, 2308–2324.

Gill, P. G., 2014: Objective verification of World Area Forecast Centre Clear Air Turbulence Forecasts. *Meteor. Appl.*, 21, 3-11, DOI: 10.1002/met.1288.

Gill, P. G., and Stirling, A. J., 2013: Introducing Convection to World Area Forecast Centre Turbulence Forecasts, *Meteor. Appl.*, 20, 107-114, DOI: 10.1002/met.1315.

International Civil Aviation Organization (ICAO), 2010: Meteorological service for international air navigation. – Annex 3 to the Convention on International Civil Aviation, 17th Edition, 206 pp. [Available online at http://store1.icao.int/index.php/publications/annexes/3-meteorological-service-for-international-air-navigation.html].

Jardin, M. R., and Bryson, A. E., 2001: Neighboring Optimal Aircraft Guidance in Winds. *J. Guid., Control Dynam.*, **24(4)**, 710–715.

Jardin, M., and Bryson, A., 2012: Methods for Computing Minimum-Time Paths in Strong Winds. *J. Aircraft*, **35(1)**, 165-171.

Janjić, Z. I., 2002: Nonsingular implementation of the Mellor-Yamada level 2.5 scheme in the NCEP Meso model. *NCEP office note*, No. 437, 61 pp.

Kim, J.-H., and H.-Y. Chun, 2010: A numerical study of clear-air turbulence (CAT) encounters over South Korea on 2 April 2007. *J. Appl. Meteor. Climatol.*, **49,** 2381-2403.

Kim, J.-H., and Chun, H.-Y., 2011: Statistics and Possible Sources of Aviation Turbulence over South Korea. *J. Appl. Meteor. Climatol.*, **50**, 311-324.

Kim, J.-H., Chun, H.-Y., Sharman, R. D., and Keller, T. L., 2011: Evaluations of Upper-Level Turbulence Diagnostics Performance Using the Graphical Turbulence Guidance (GTG) System and Pilot Reports (PIREPs) over East Asia. *J. Appl. Meteor. Climatol.*, **50**, 1936-1951.

Kim, J.-H., and Chun, H.-Y., 2012: A Numerical Simulation of Convectively Induced Turbulence above Deep Convection. *J. Appl. Meteor. Climatol.*, **51**, 1180-1200.

Kim, J.-H., Chun, H.-Y., Sharman, R. D., and Trier, S. B., 2014: The Role of Vertical Shear on Aviation Turbulence within Cirrus Bands of a Simulated Western Pacific

Ocean. *Mon. Wea. Rev.*, **142**, 2794-2813.

Knox, J. A., D. W. McCann, and P. D. Williams, 2008: Application of the Lighthill–Ford theory of spontaneous imbalance to clear-air turbulence forecasting. *J. Atmos. Sci.*, **65**, 3292–3304.

Krozel, J., Klimenko, V., and Sharman, R. D., 2011: Analysis of Clear-Air Turbulence Avoidance Maneuvers. *Air Traffic Control Quart.*, **4(2)**, 147-168.

Lane, T. P. and R. D. Sharman, 2008: Some influences of background flow conditions on the generation of turbulence due to gravity wave breaking above deep convection. *J. Appl. Meteor. Climatol.*, **47**, 2777–2796.

Lane, T. P. and R. D. Sharman, 2014: Intensity of thunderstorm-generated turbulence revealed by large-eddy simulation. *Geophys. Res. Lett.*, **41**(6), 2221–2227. DOI: 10.1002/2014GL059299.

Lane, T. P., R. D. Sharman, T. L. Clark, and H.-M. Hsu, 2003: An investigation of turbulence generation mechanisms above deep convection. *J. Atmos. Sci.*, **60**, 1297-1321.

Lane, T. P., J. D. Doyle, R. Plougonven, M. A. Shapiro, and R. D. Sharman, 2004: Observations and numerical simulations of inertia–gravity waves and shearing instabilities in the vicinity of a jet stream. *J. Atmos. Sci.*, **61**, 2692–2706.

Lane, T. P., J. D. Doyle, R. D. Sharman, M. A. Shapiro, and C. D. Watson, 2009: Statistics and dynamics of aircraft encounters of turbulence over Greenland. *Mon. Wea. Rev.*, **137**, 2687–2702.

Lane, T. P., Sharman, R. D., Trier, S. B., Fovell, R. G., and Williams, J. K., 2012: Recent Advances in the Understanding of Near-Cloud Turbulence. *Bull. Amer. Meteor. Soc.*, **93(4)**, 499-515.

Lester, P. F., 1994: *Turbulence: A New Perspective for Pilots*. Jeppesen Sanderson, 212 pp.

Lindborg, E., 1999: Can the atmospheric kinetic energy spectrum be explained by two-dimensional turbulence? *J. Fluid Mech.*, **388(6)**, 259–288.

Mlawer, E. J., S. J. Taubman, P. D. Brown, M. J. Iacono, and S. A. Clough, 1997: Radiative transfer for inhomogeneous atmosphere: RRTM, a validated correlated-k model for the longwave. *J. Geophys. Res.*, **102 (D14)**, 16663–16682.

McNally, D., Sheth, K., Gong, C., Love, J., Lee, C. H., Sahlman, S., and Cheng, J., 2012: Dynamic Weather Routes: a Weather Avoidance System for Near-Term Trajectory-Based Operations. *28th International Congress of the Aeronautical Sciences (ICAS)*, Brisbane, Australia.

Mellor, G. L., and T. Yamada, 1982: Development of a turbulence closure model for geophysical fluid problems. *Rev. Geophys. Space Phys.*, **20**, 851–875.

Ng. H. K., Grabbe, S., and Mukherjee, A., 2009: Design and Evaluation of a Dynamic Programming Flight Routing Algorithm Using the Convective Weather Avoidance Model. AIAA-2009-5862*, AIAA Guidance, Navigation, and Control Conference*, Chicago, IL.

Ng, H. K., Sridhar, B., Grabbe, S., and Chen, N., 2011: Cross-polar aircraft trajectory optimization and the potential climate impact. *30th Digital Avionics Systems Conference (DASC)*, Seattle, WA.

Ng, H. K., Sridhar, B., and Grabbe, S., 2012: A Practical Approach for Optimizing Aircraft Trajectories in Winds. *31st Digital Avionics Systems Conference*, Institute of Electrical and Electronics Engineers, Williamsburg, VA.

Palopo, K., Windhorst, R. D., Suharwardy, S., and Lee, H.-T., 2010: Wind Optimal

Routing in the National Airspace System. *J. Aircraft*, **47(5)**, 1584-1592.

Reap, R. M., 1996: Probability Forecasts of Clear-Air Turbulence for the Contiguous U.S. National Weather Service Office of Meteorology Tech., Procedures Bulletin, 430, 15 pp.

Roach, W. T., 1970: On the influence of synoptic development on the production of high level turbulence. *Quart. J. Roy. Meteor. Soc.*, **96**, 413–429.

Skamarock, W. C. and Klemp, J. B., 2007: A Time-Split Nonhydrostatic Atmospheric Model for Weather Research and Forecasting Applications. *J. Comput. Phys.*, **227(7)**, 3465-3485.

Sharman, R. D., Tebaldi, C., Wiener, G., and Wolff, J., 2006: An Integrated Approach to Mid- and Upper-Level Turbulence Forecasting. *Wea. Forecasting*, **21(3)**, 268-287.

Sharman, R. D., S. B. Trier, T. P. Lane, and J. D. Doyle, 2012: Sources and dynamics of turbulence in the upper troposphere and lower stratosphere: A review. *Geophys. Res. Lett.*, **39,** L12803.

Sharman, R. D., Doyle, J. D., Shapiro, M. A., 2011: An Investigation of a Commercial Aircraft Encounter with Severe Clear-Air Turbulence over Western Greenland. *J. Appl. Meteor. Climatol.*, **51(1)**, 311-324.

Sharman, R. D., 2013: New Developments in the Graphical Turbulence Guidance Product. Preprint, *Workshop on Aviation Turbulence*, Boulder, CO.

Sharman, R. D., L. B. Cornman, G. Meymaris, J. Pearson, T. Farrar, 2014: Description and Derived Climatologies of Automated In Situ Eddy-Dissipation-Rate Reports of Atmospheric Turbulence. *J. Appl. Meteor. Climatol.*, **53**, 1416–1432. doi: http://dx.doi.org/10.1175/JAMC-D-13-0329.1.

Smirnova, T. G., J. M. Brown, S. G. Benjamin, and D. Kim, 2000: Parameterization of coldseason processes in the MAPS land-surface scheme. *J. Geophys. Res.*, **105** (D3), 4077–4086.

Sridhar, B., Ng, H. K., and Chen, N. Y., 2010: Aircraft Trajectory Optimization and Contrails Avoidance in the Presence of Winds. *10th AIAA Aviation Technology, Integration, and Operations (ATIO) conference*, Fort Worth, TX.

Steiner M., Bateman, R., Megenhardt, D., Liu, Y., Pocernich, M., and Krozel, J., 2010: Translation of Ensemble Weather Forecasts into Probabilistic Air Traffic Capacity Impact. *Air Traffic Control Quart.*, **18(3)**, 229-254.

Thompson, G., R. M. Rasmussen, and K. Manning, 2004: Explicit forecasts of winter precipitation using an improved bulk microphysics scheme. Part I: Description and sensitivity analysis. *Mon. Wea. Rev.*, **132**, 519–542

Trier, S. B. and Sharman, R. D., 2009: Convection-Permitting Simulations of the Environment Supporting Widespread Turbulence within the Upper-Level Outflow of a Mesoscale Convective System. *Mon. Wea. Rev.*, **137(6)**, 1972-1990.

Trier, S. B., Sharman, R. D., Fovell, R. G., and Frehlich, R. G., 2010: Numerical Simulation of Radial Cloud Bands within the Upper-Level Outflow of an Observed Mesoscale Convective System. *J. Atmos. Sci.*, **67(9)**, 2990-2999.

Williams, P. D. and M. M. Joshi, 2013: Intensification of winter transatlantic aviation turbulence in response to climate change. *Nature Clim. Change*, **3(7)**, 644-648.

Table Captions

Table 1. 2×2 contingency table for the probability-of-detection (POD) statistics methodology at the given threshold.

Table 2. AUC (area under the curve) values of the PODY-PODN statistics/RMSE (Root Mean Square Error) for ten EDR-scale turbulence metrics from different weather forecasts (1.5-5.5 hr forecast) against in situ EDR measurements over the CONUS during two periods (7-8 September 2012 and 31 December 2011) and an example of the weighting values for the time-lagged ensemble EDR 1 using 1.5-3.5 hrs forecasts derived from Eq. (5) is in the rightmost columns.

Table 3. Minutes of the total travel time (left column), additional flight time along the LTAR compared to Wind-Optimal Route (middle column), and flight time in areas of SOG probability > 10% along the LTARs from the Los Angeles international airport (LAX) to John F. Kennedy (JFK) international airport. Geographical paths of the LTAR1, LTAR2, and LTAR3 are shown as red line in Fig. 8 (upper), green line in Fig. 8 (middle), and green line in Fig. 8 (lower), respectively.

Figure Captions

Figure 1. Echo top (×1000 ft) over the Continuous United States (CONUS), obtained from interpolating the raw 1-km Corridor Integrated Weather System (CIWS) analyses data (mosaic of the ground-based WSR-88 radar reflectivity) to 3-km grid at observation times of (a) 1730 UTC and (b) 2230 UTC 7 September 2013, and derived from 2.5-hr forecast data of Weather Research and Forecast (WRF) with 3-km horizontal grid spacing valid at (c) 1730 UTC 7 and (d) 2230 UTC 7 September 2013. Locations of turbulence encounters measured by *in situ* Eddy Dissipation Rate (EDR > 0.22 $m^{2/3}$ s^{-1}) are depicted as red asterisks in all plots. Note that the coverage of WSR-88 radar mosaic is within gray-blue areas in (a) and (b), which is out of range for the storms in northern Mexico and Gulf of Mexico shown in (c) and (d).

Figure 2. (a) and (b) the same as Figs. 1(a) and 1(c) except at 1830 UTC 31 December 2011. (c) Terrain height (shading; km) with horizontal wind vectors (m s^{-1}) averaged using three layers of FL300, FL350, and FL400 and (d) vertical velocity (m s^{-1}) at FL350, derived from 2.5-hr WRF forecast valid at 1830 UTC 7 September 2012. As in Fig 1., locations of turbulence encounters measured by in situ EDR (> 0.22 $m^{2/3}$ s^{-1}) are also depicted as red (a, b, and d) and white (c) asterisks in all plots.

Figure 3. An example of snapshots of nine EDR-scale turbulence metrics (SGS TKE/Ri, FS EDR/Ri, DEFSQ/Ri, ADIV/Ri, VRTSQ/Ri, |w|/Ri, F2D/Ri, BR1/Ri, and NGM/Ri) derived from 2.5-hr forecast data of WRF-ARW model, averaged three layers of FL300, FL350, and FL400 valid at 1730 UTC 7 September 2012.

Observed *in situ* EDR locations are also depicted as gray (EDR > 0.01 $m^{2/3}$ s^{-1}) and blue (EDR > 0.22 $m^{2/3}$ s^{-1}) dots in all plots.

Figure 4. The same as Fig. 3 except at 1830 UTC 31 December 2011.

Figure 5. Deterministic ensemble EDR (left) and probabilistic ensemble EDR for Severe-Or-Greater (SOG)-level turbulence (right), averaged using three layers of FL300, FL350, and FL400 derived from 1.5-3.5 hr time-lagged weather forecasts valid at 1730 UTC 7 September 2012 (upper) and 1830 UTC 31 December 2011 (lower). Observed *in situ* EDR measurements (> 0.22 $m^{2/3}$ s^{-1}) (blue asterisks) are also depicted in all plots. Note that the color shadings in the left and right panels are different.

Figure 6. X-Y plots for the PODY and PODN statistics of the (left) DEFSQ/Ri metrics from 1.5-hr (purple dashed line), 2.5-hr (orange dash-dot-dotted line), 3.5-hr (blue dash-dotted line), 4.5-hr (green dotted line), and 5.5-hr (red long dashed line) forecast data and (right) EDR-scale turbulence metrics (SGS TKE/Ri; purple dashed line, FS EDR/Ri; orange dash-dot-dotted line, DEFSQ/Ri; blue dash-dotted line, ADIV/Ri; green dotted line, VORTSQ/Ri; red long dashed line) from 2.5-hr forecast data, compared with the observed *in situ* EDR measurements for 7-8 September 2012 (upper) and for 31 December 2011 (middle), and for both periods (lower). Those for time-lagged ensemble EDR 1 using 1.5-3.5 hrs data (blue bold-solid line), 2 using 2.5-4.5 hrs data (red bold-solid line), and 3 using 3.5-5.5 hrs (black bold-solid line) are also depicted in all plots.

Figure 7. (a and b) Probabilistic ensemble EDR for SOG-level turbulence with horizontal wind vectors, Wind-Optimal Route (WOR; blue line), and Great Circle Route with wind (sky-blue line) from Los Angeles international airport (LAX) to

John F. Kennedy international airport (JFK) using 2.5-hr forecasted wind from the WRF-ARW model and (c and d) vertical cross-sections for probabilistic ensemble EDR for Severe-Or-Greater (SOG)-level turbulence along the WOR valid at (left) 1730 UTC 7 September 2012 and (right) 1830 UTC 31 December 2011. Reference wind vector in a and b is 30 m s^{-1}. Locations of departure (LAX) and arrival (JFK) are also depicted as blue dots in a and b.

Figure 8. (Upper) Probabilistic ensemble EDR forecast for SOG-level turbulence with horizontal wind vectors and Wind-Optimal Routes (WORs; blue lines) and Lateral Turbulence Avoidance Route (LTAR; red line) at FL350 from Los Angeles international airport (LAX) to John F. Kennedy international airport (JFK) using 3.5-5.5 hr forecasts valid at 1730 UTC 9 Sep 2010. Middle and lower panels are the same as upper panel except for the LTARs (green lines) initiated after 1.5-hr (middle) and 2.5-hr (lower) departing from LAX along the WOR (blue lines) between LAX to JFK using 2.5-4.5 hr forecasts (middle) and using 1.5-3.5 hr forecasts (lower) valid at 1730 UTC 9 September 2010.

Table 1. 2×2 contingency table for the probability-of-detection (POD) statistics methodology at the given threshold.

	Observation (obs)	
Forecast (for)	Yes	No
Yes	$Y_{for}Y_{obs}$	$Y_{for}N_{obs}$
No	$N_{for}Y_{obs}$	$N_{for}N_{obs}$

Table 2. AUC (area under the curve) values of the PODY-PODN statistics/RMSE (Root Mean Square Error) for ten EDR-scale turbulence metrics from different weather forecasts (1.5-5.5 hr forecast) against in situ EDR measurements over the CONUS during two periods (7-8 September 2012 and 31 December 2011) and an example of the weighting values for the time-lagged ensemble EDR 1 using 1.5-3.5 hrs forecasts derived from Eq. (5) is in the rightmost columns.

Metrics	1.5-hr	2.5-hr	3.5-hr	4.5-hr	5.5-hr	Wt. 1.5-hr	Wt. 2.5-hr	Wt. 3.5-hr
SGS TKE/Ri	0.736 / 0.037	0.737 / 0.038	0.710 / 0.039	0.725 / 0.040	0.713 / 0.041	0.0189	0.0187	0.0175
FS EDR/Ri	0.827 / 0.013	0.837 / 0.016	0.834 / 0.017	0.812 / 0.018	0.822 / 0.019	0.1378	0.1160	0.1076
DEFSQ/Ri	0.821 / 0.030	0.811 / 0.033	0.804 / 0.035	0.784 / 0.037	0.797 / 0.039	0.0295	0.0256	0.0236
ADIV/Ri	0.785 / 0.034	0.793 / 0.036	0.775 / 0.038	0.786 / 0.040	0.792 / 0.042	0.0230	0.0223	0.0202
VORTSQ/Ri	0.739 / 0.024	0.731 / 0.026	0.731 / 0.027	0.712 / 0.028	0.733 / 0.030	0.0417	0.0359	0.0344
|w|/Ri	0.780 / 0.034	0.775 / 0.036	0.764 / 0.037	0.777 / 0.039	0.791 / 0.040	0.0237	0.0231	0.0220
F2D/Ri	0.755 / 0.051	0.777 / 0.056	0.758 / 0.058	0.741 / 0.060	0.739 / 0.061	0.0096	0.0087	0.0084
Brown1/Ri	0.819 / 0.029	0.820 / 0.031	0.804 / 0.032	0.782 / 0.034	0.786 / 0.036	0.0356	0.0304	0.0279
NGM/Ri	0.820 / 0.028	0.827 / 0.030	0.820 / 0.031	0.808 / 0.033	0.818 / 0.034	0.0402	0.0349	0.0337
HTG/Ri	0.750 / 0.054	0.768 / 0.056	0.756 / 0.058	0.754 / 0.060	0.757 / 0.061	0.0096	0.0089	0.0086

Table 3. Minutes of the total travel time (left column), additional flight time along the LTAR compared to Wind-Optimal Route (middle column), and flight time in areas of SOG probability > 10% along the LTARs from the Los Angeles international airport (LAX) to John F. Kennedy (JFK) international airport. Geographical paths of the LTAR1, LTAR2, and LTAR3 are shown as red line in Fig. 8 (upper), green line in Fig. 8 (middle), and green line in Fig. 8 (lower), respectively.

	Flight time (minutes)		
Types of the flight routes	Total flight from LAX to JFK	Additional time compared to WOR	Flight time in areas of SOG > 10%
WOR	*238*	*0*	*52*
LTAR1	*254*	*16*	*0*
LTAR2	***244***	***6***	*0*
LTAR3	*256*	*18*	*0*

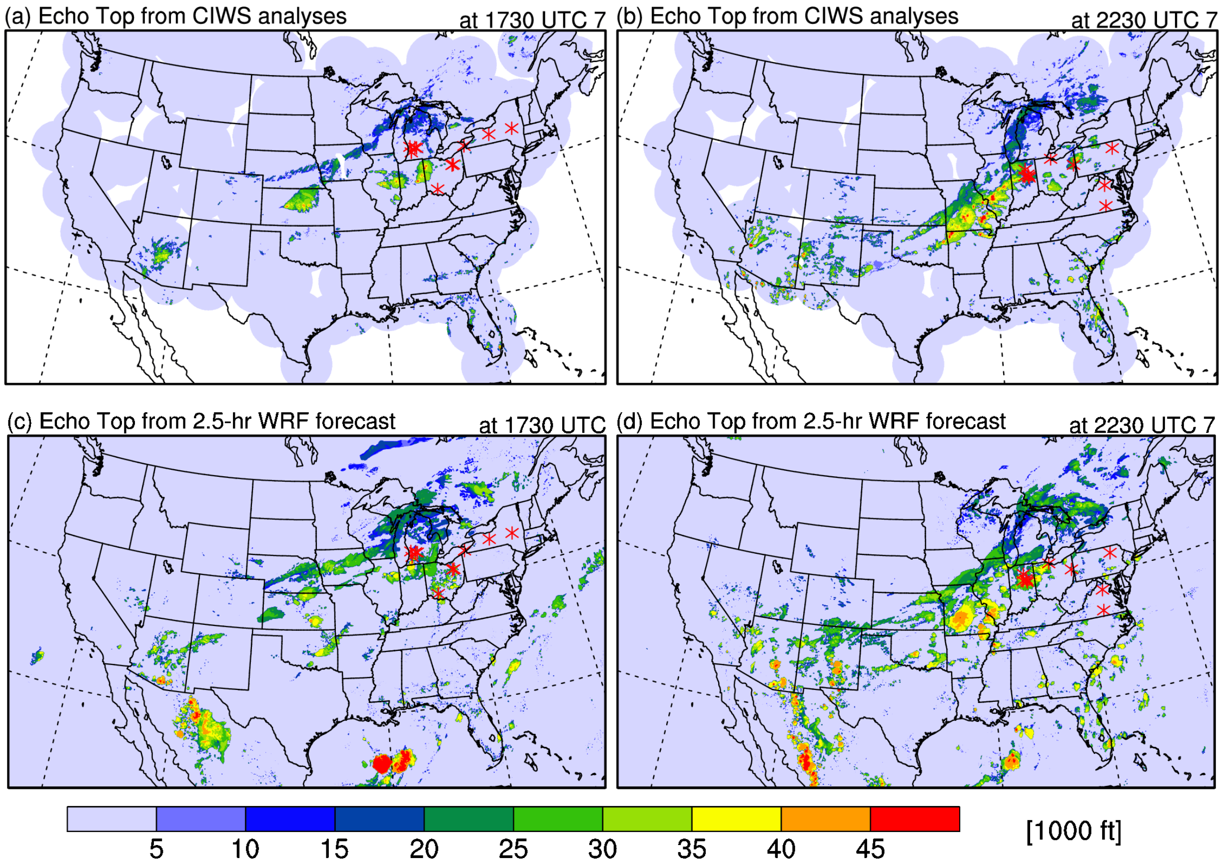

Figure 1. Echo top (×1000 ft) over the Continuous United States (CONUS), obtained from interpolating the raw 1-km Corridor Integrated Weather System (CIWS) analyses data (mosaic of the ground-based WSR-88 radar reflectivity) to 3-km grid at observation times of (a) 1730 UTC and (b) 2230 UTC 7 September 2013, and derived from 2.5-hr forecast data of Weather Research and Forecast (WRF) with 3-km horizontal grid spacing valid at (c) 1730 UTC 7 and (d) 2230 UTC 7 September 2013. Locations of turbulence encounters measured by *in situ* Eddy Dissipation Rate (EDR ≥ 0.22 $m^{2/3}$ s^{-1}) are depicted as red asterisks in all plots. Note that the coverage of WSR-88 radar mosaic is within gray-blue areas in (a) and (b), which is out of range for the storms in northern Mexico and Gulf of Mexico shown in (c) and (d).

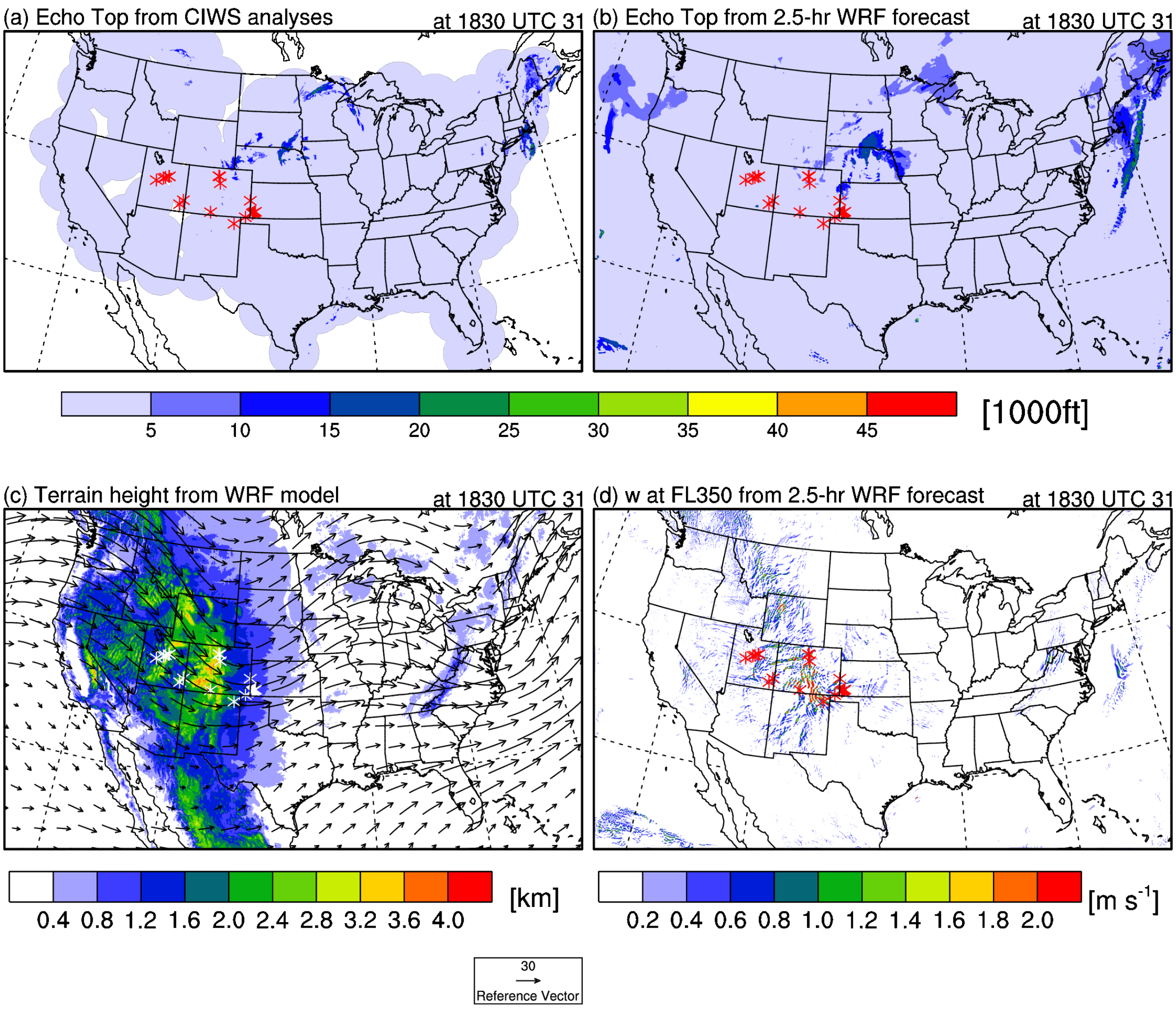

Figure 2. (a) and (b) the same as Figs. 1(a) and 1(c) except at 1830 UTC 31 December 2011. (c) Terrain height (shading; km) with horizontal wind vectors (m s^{-1}) averaged using three layers of FL300, FL350, and FL400 and (d) vertical velocity (m s^{-1}) at FL350, derived from 2.5-hr WRF forecast valid at 1830 UTC 7 September 2012. As in Fig 1., locations of turbulence encounters measured by in situ EDR (≥ 0.22 $m^{2/3}$ s^{-1}) are also depicted as red (a, b, and d) and white (c) asterisks in all plots.

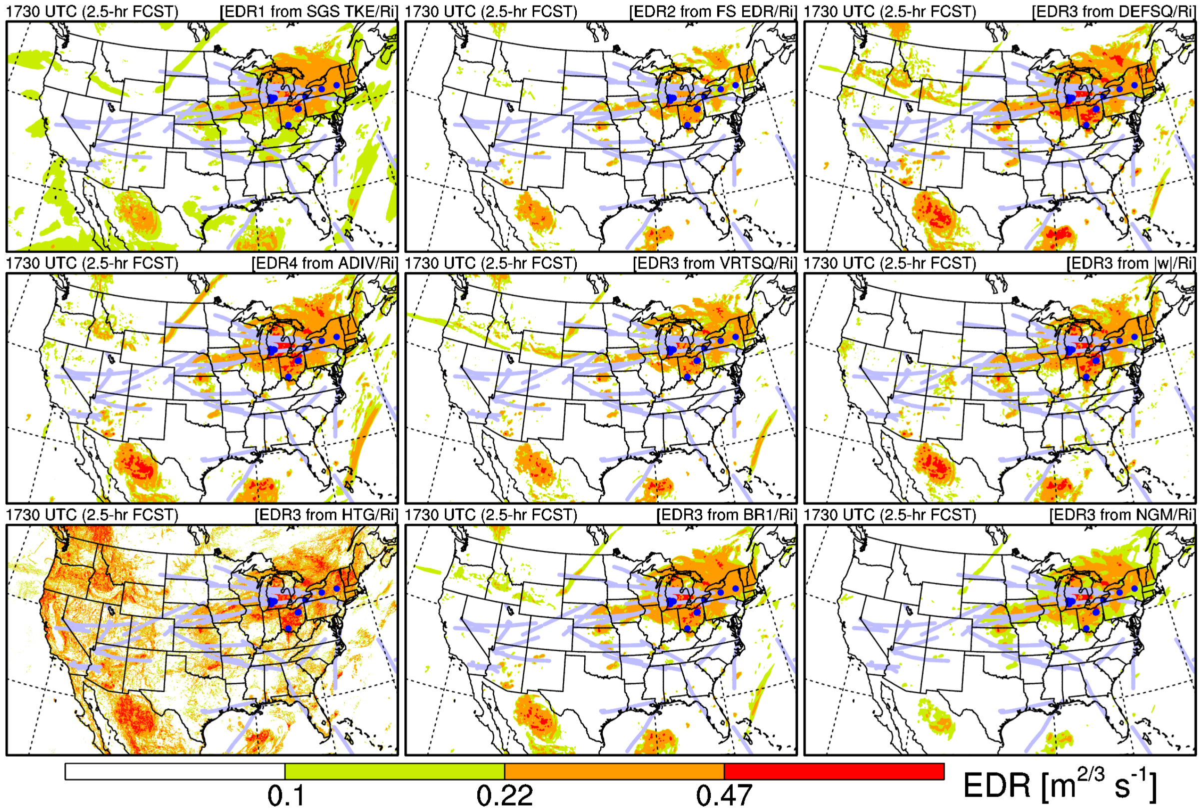

Figure 3. An example of snapshots of nine EDR-scale turbulence metrics (SGS TKE/Ri, FS EDR/Ri, DEFSQ/Ri, ADIV/Ri, VRTSQ/Ri, |w|/Ri, HTG/Ri, BR1/Ri, and NGM/Ri) derived from 2.5-hr forecast data of WRF-ARW model, averaged three layers of FL300, FL350, and FL400 valid at 1730 UTC 7 September 2012. Observed *in situ* EDR locations are also depicted as gray (EDR ≤ 0.01 $m^{2/3}$ s^{-1}) and blue (EDR ≥ 0.22 $m^{2/3}$ s^{-1}) dots in all plots.

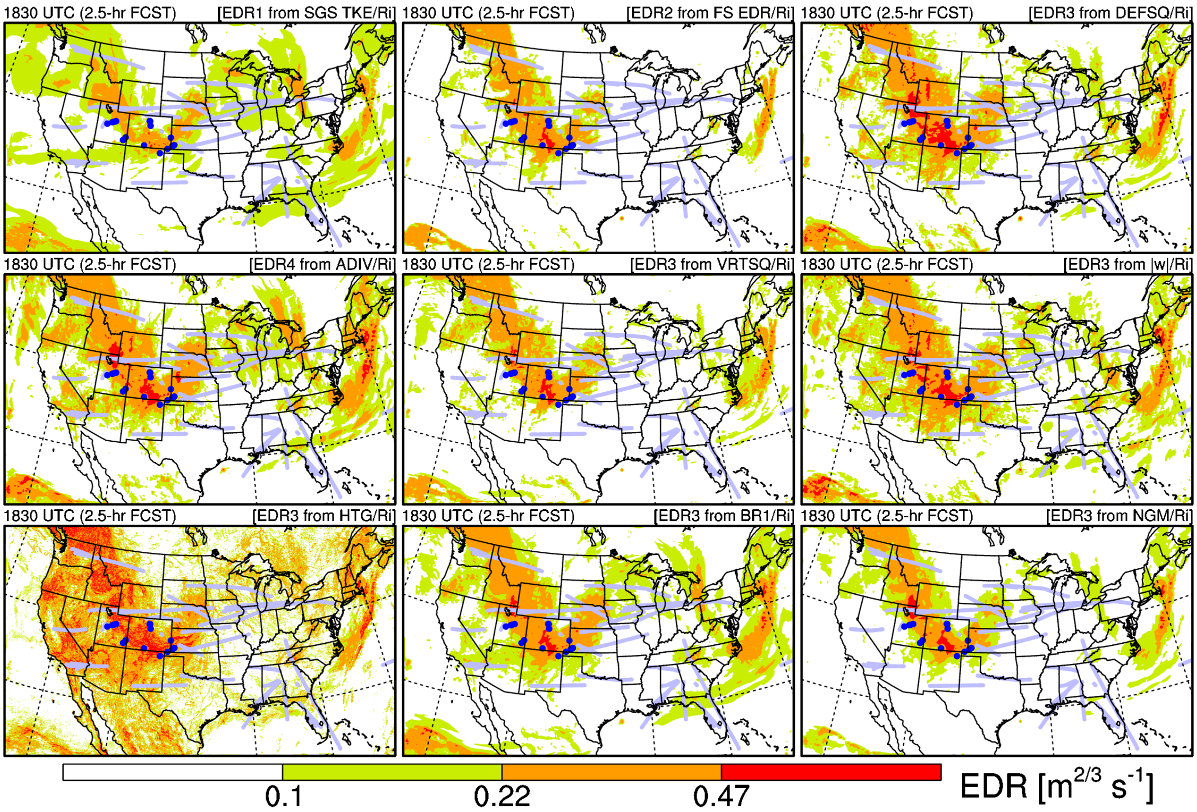

Figure 4. The same as Fig. 3 except at 1830 UTC 31 December 2011.

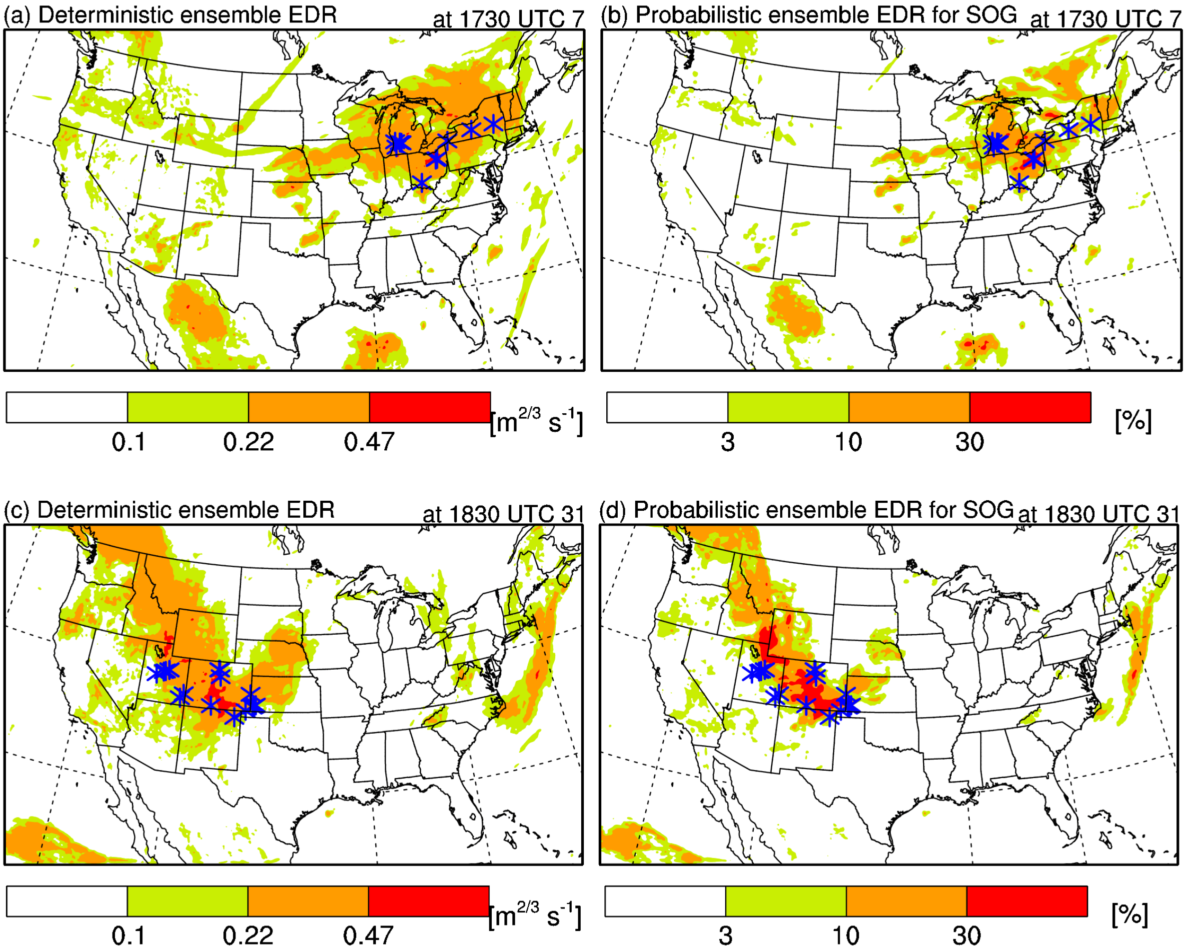

Figure 5. Deterministic ensemble EDR (left) and probabilistic ensemble EDR for Severe-Or-Greater (SOG)-level turbulence (right), averaged using three layers of FL300, FL350, and FL400 derived from 1.5-3.5 hr time-lagged weather forecasts valid at 1730 UTC 7 September 2012 (upper) and 1830 UTC 31 December 2011 (lower). Observed *in situ* EDR measurements (≥ 0.22 m$^{2/3}$ s^{-1}) (blue asterisks) are also depicted in all plots. Note that the color shadings in the left and right panels are different.

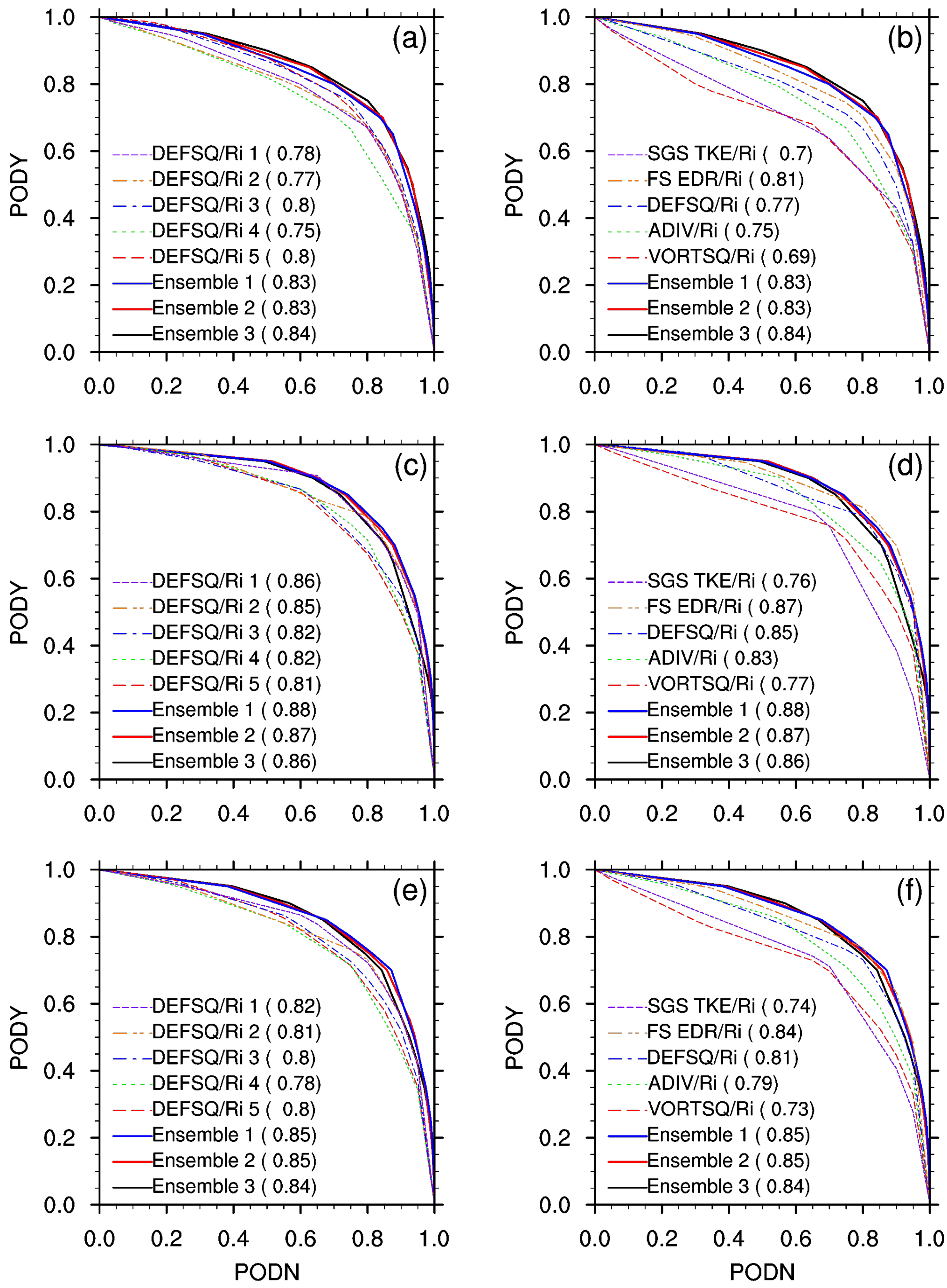

Figure 6. X-Y plots for the PODY and PODN statistics of the (left) DEFSQ/Ri metrics from 1.5-hr (purple dashed line), 2.5-hr (orange dash-dot-dotted line), 3.5-hr (blue dash-dotted line), 4.5-hr (green dotted line), and 5.5-hr (red long dashed line) forecast data and (right) EDR-scale turbulence metrics (SGS TKE/Ri; purple dashed line, FS EDR/Ri; orange dash-dot-dotted line, DEFSQ/Ri; blue dash-dotted line, ADIV/Ri; green dotted line, VORTSQ/Ri; red long dashed line) from 2.5-hr forecast data, compared with the observed *in situ* EDR measurements for 7-8 September 2012 (upper) and for 31 December 2011 (middle), and for both periods (lower). Those for time-lagged ensemble EDR 1 using 1.5-3.5 hrs data (blue bold-solid line), 2 using 2.5-4.5 hrs data (red bold-solid line), and 3 using 3.5-5.5 hrs (black bold-solid line) are also depicted in all plots.

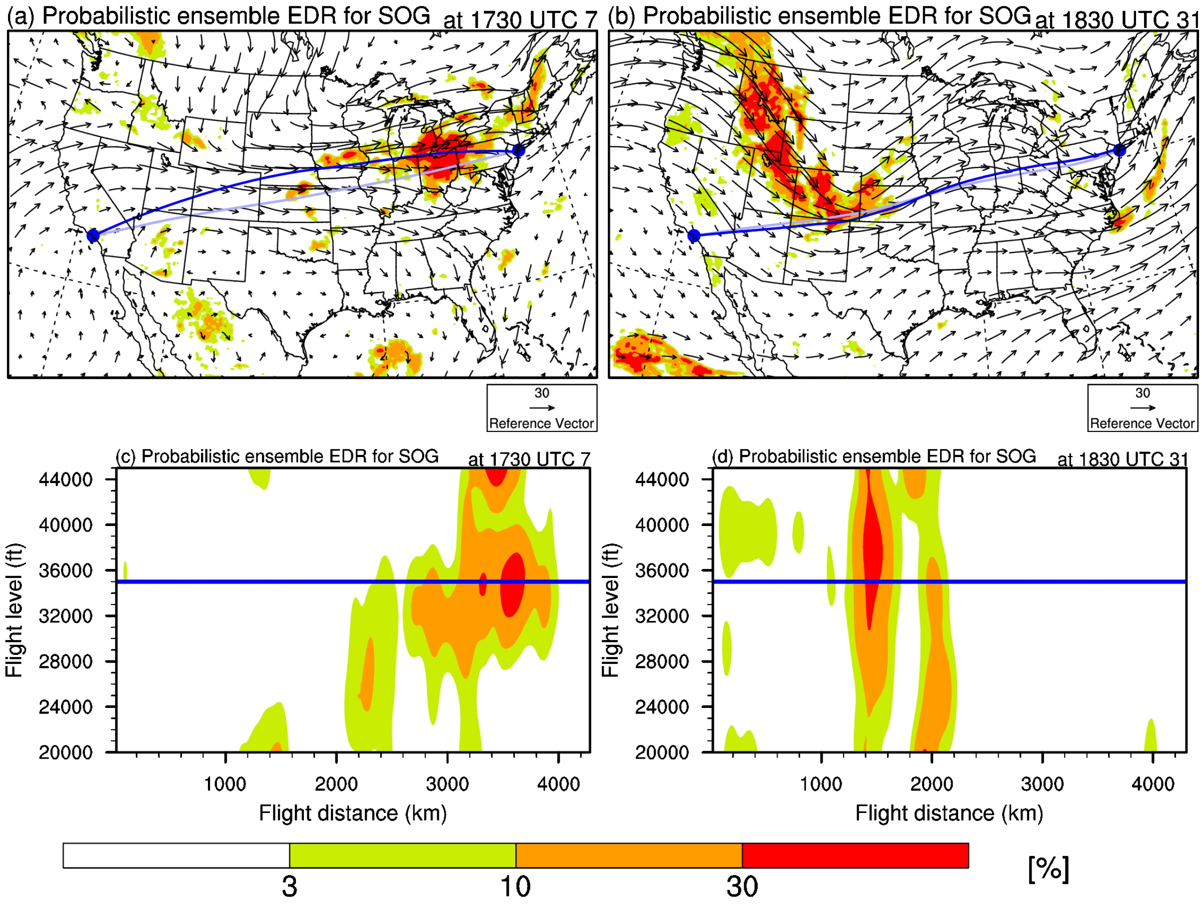

Figure 7. (a and b) Probabilistic ensemble EDR for SOG-level turbulence with horizontal wind vectors, Wind-Optimal Route (WOR; blue line), and Great Circle Route with wind (sky-blue line) from Los Angeles international airport (LAX) to John F. Kennedy international airport (JFK) using 2.5-hr forecasted wind from the WRF-ARW model and (c and d) vertical cross-sections for probabilistic ensemble EDR for Severe-Or-Greater (SOG)-level turbulence along the WOR valid at (left) 1730 UTC 7 September 2012 and (right) 1830 UTC 31 December 2011. Reference wind vector in a and b is 30 m s^{-1}. Locations of departure (LAX) and arrival (JFK) are also depicted as blue dots in a and b.

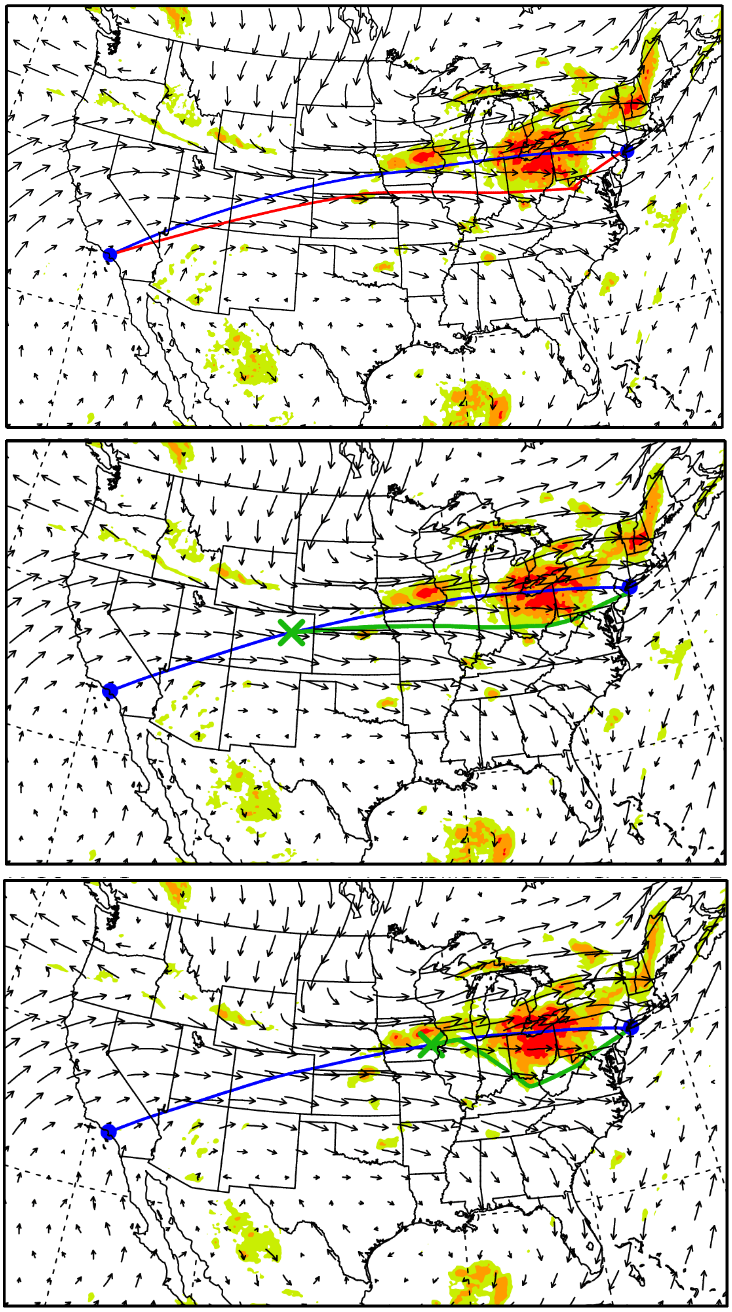

Figure 8. (Upper) Probabilistic ensemble EDR forecast for SOG-level turbulence with horizontal wind vectors and Wind-Optimal Routes (WORs; blue lines) and Lateral Turbulence Avoidance Route (LTAR; red line) at FL350 from Los Angeles international airport (LAX) to John F. Kennedy international airport (JFK) using 3.5-5.5 hr forecasts valid at 1730 UTC 9 Sep 2010. Middle and lower panels are the same as upper panel except for the LTARs (green lines) initiated after 1.5-hr (middle) and 2.5-hr (lower) departing from LAX along the WOR (blue lines) between LAX to JFK using 2.5-4.5 hr forecasts (middle) and using 1.5-3.5 hr forecasts (lower) valid at 1730 UTC 9 September 2010.